Family of dual topological materials $X\mathrm{Sb_4Te_4}$ (X = Ge, Sn, Pb)

M. Bosnar,[1,2,*] A.Yu. Vyazovskaya,[3,4] I.Yu. Sklyadneva,[1] S. V. Eremeev,[5] Yu. M. Koroteev,[5] E. K. Petrov,[3,4] R. Heid,[6] R. M. Geilhufe,[7] A. Ernst,[8,9] E. V. Chulkov,[1,4,10] and M. M. Otrokov[11,†]

[1]*Donostia International Physics Center, 20018 Donostia-San Sebastián, Spain*

[2]*Departamento de Polímeros y Materiales Avanzados: Física, Química y Tecnología, Facultad de Ciencias Químicas, Universidad del País Vasco UPV/EHU, 20018 Donostia-San Sebastián, Spain*

[3]*Tomsk State University, 634050 Tomsk, Russia*

[4]*Saint Petersburg State University, 199034 Saint Petersburg, Russia*

[5]*Institute of Strength Physics and Materials Science, Russian Academy of Sciences, 634021 Tomsk, Russia*

[6]*Institute for Quantum Materials and Technologies, Karlsruhe Institute of Technology, D-76021 Karlsruhe, Germany*

[7]*Department of Physics, Chalmers University of Technology, 41296 Göteborg, Sweden*

[8]*Institut für Theoretische Physik, Johannes Kepler Universität, A 4040 Linz, Austria*

[9]*Max-Planck-Institut für Mikrostrukturphysik, Weinberg 2, D-06120, Halle, Germany*

[10]*Centro de Física de Materiales (CFM-MPC), Centro Mixto (CSIC-UPV/EHU), 20018 Donostia-San Sebastián, Spain*

[11]*Instituto de Nanociencia y Materiales de Aragón (INMA), CSIC-Universidad de Zaragoza, Zaragoza 50009, Spain*

(Received 4 October 2024; accepted 13 December 2024; published 14 January 2025)

Using density functional theory, we characterize crystal and electronic structures as well as the topology of the $X\mathrm{Sb_4Te_4}$ family of materials (X = Ge, Sn, Pb) that are composed of the $X\mathrm{Sb_2Te_4}$ septuple layers interleaved by Sb bilayers. We first demonstrate that all these compounds are dynamically stable by means of phonon spectra calculations. Then, our electronic structure calculations, performed within the modified Becke-Johnson potential approximation, predict $\mathrm{GeSb_4Te_4}$ and $\mathrm{SnSb_4Te_4}$ to be semimetals, while $\mathrm{PbSb_4Te_4}$ to be an insulator with a narrow gap of about 50 meV. Further, we find all $X\mathrm{Sb_4Te_4}$ to show both the strong $\mathbb{Z}_2$ topology and the crystalline topology provided by the time-reversal and mirror reflection symmetries, respectively. We demonstrate the stability of this dual topological nature with respect to a considerable X-Sb intermixing previously found experimentally.

DOI: 10.1103/PhysRevMaterials.9.014201

I. INTRODUCTION

Topological materials have been attracting a great deal of attention during the past two decades due to their exotic properties and significant applied potential [1–4]. The key role in the topologically nontrivial matter is played by spin-orbit coupling (SOC), which, in combination with various symmetries and properties (e.g., magnetism or superconductivity) gives rise to various topological phases [5–8]. The most widely studied class of topological materials are time-reversal symmetric (nonmagnetic) topological insulators (TIs). In these systems, SOC causes inversion of the fundamental bulk band gap, which leads to the appearance of the special gapless surface states, connecting the bulk valence and conduction bands. The nontrivial bulk topology makes them robust against external perturbations, while their helical spin texture protects surface electrons from the elastic back-scattering, rendering these materials attractive for dissipationless transport applications.

There, however, exist materials that are both time-reversal and crystalline symmetric TIs. It is said that they feature a dual topology [9]. In such systems, the time-reversal and crystalline symmetries may protect either the same or different topological surface states (TSSs). The former case corresponds typically to the strong $\mathbb{Z}_2$ 3D TIs, such as $\mathrm{Bi_2Te_3}$ [9], whose TSS at (0001) surface is protected not only by the TRS but also by the reflection symmetry with respect to the $\{1\bar{1}00\}$ mirror planes. The latter case is that of weak $\mathbb{Z}_2$ TIs, featuring TSS at the non-mirror-symmetric surfaces, while the reflection symmetry protects the TSS at the surfaces that are free of the TRS-protected 2D states. This situation was found to occur in, e.g., the $m\mathrm{Bi_{BL}} \cdot n(\mathrm{Bi_2Te_3})_{\mathrm{QL}}$ superlattices composed of Bi bilayers (BLs) and $\mathrm{Bi_2Te_3}$ quintuple layers (QLs), such as $\mathrm{Bi_4Te_3}$ ($m, n = 1$) [10] or $\mathrm{Bi_1Te_1}$ ($m = 1, n = 2$) [11], as well as in heterostructures consisting of two mirrored BiTeI trilayers and a Bi BL [12].

Indeed, the dual topological materials based on natural superlattices of the $m\mathrm{Bi_{BL}} \cdot n(\mathrm{Bi_2Te_3})_{\mathrm{QL}}$ type have been receiving increasing attention lately: the electronic structure of various members of the family has been experimentally studied by angle-resolved photoemission spectroscopy [10,11,13–17] and transport measurements [17]. In contrast, their Sb-based counterparts received much less attention, be it in the form of bulk single crystals or films grown by molecular-beam epitaxy [18–20]. Another unexplored direction, to the best of our knowledge, is dual TIs based on the $XY_2\mathrm{Te_4}$ (X = Ge, Sn, Pb, Y = Bi, Sb) septuple layer (SL) blocks, instead of the QL ones.

In this work, we thus explore the Sb-based subfamily of the $Y_{\mathrm{BL}} \cdot (XY_2\mathrm{Te_4})_{\mathrm{SL}}$ superlattice family, i.e., the ternary

*Contact author: mihovil.bosnar@gmail.com
†Contact author: mikhail.otrokov@unizar.es

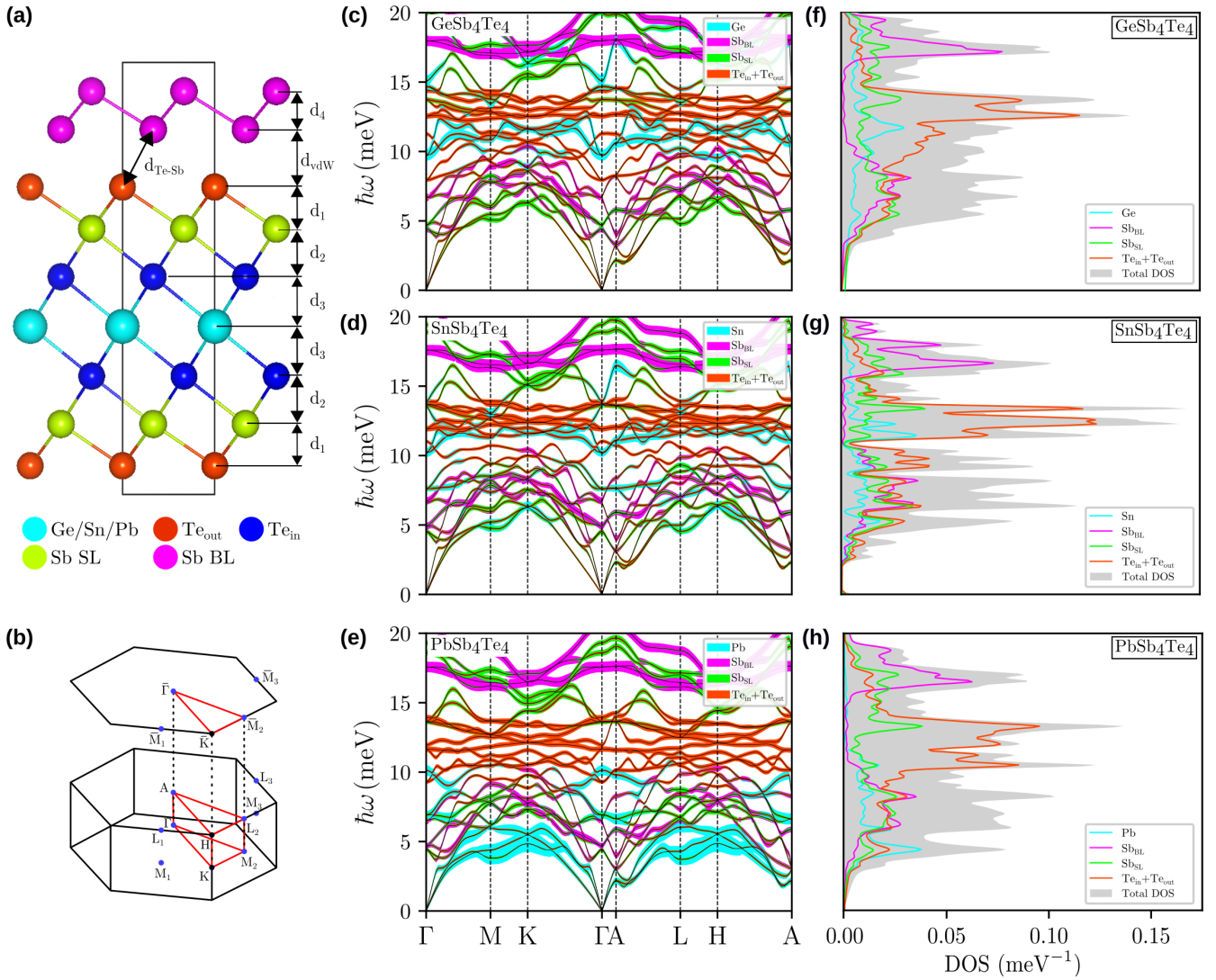

FIG. 1. (a) Ball-and-stick model of the ideal $X\mathrm{Sb_4Te_4}$ bulk crystal structure (X = Ge, Sn, Pb). (b) 3D Brillouin zone corresponding to the cell in (a), along with its 2D projection. The high symmetry points are denoted by circles, with time-reversal invariant momenta (TRIM) used for the $\mathbb{Z}_2$ invariant calculations marked in blue. (c)–(e) Phonon dispersions, calculated along the high-symmetry path shown in (b), for the ideal $X\mathrm{Sb_4Te_4}$, X = Ge (c), Sn (d), and Pb (e). The colors reflect modes contributed by different atoms: cyan–X, green–Sb-SL, red–all Te atoms, and magenta–Sb-BL. The corresponding phonon densities of states (DOS) are shown in panels (f)–(h).

compounds with the chemical formula $X\mathrm{Sb_4Te_4}$, in which the $X\mathrm{Sb_2Te_4}$ SLs are interleaved with Sb BLs. In general, the $XY_4\mathrm{Te_4}$ family has only two experimentally synthesized representatives so far, $\mathrm{GeBi_4Te_4}$ [21,22] and $\mathrm{GeSb_4Te_4}$ [23], but the topology of neither of them has been investigated yet. Therefore, we perform an exhaustive characterization of the structural, electronic, and topological properties of the $X\mathrm{Sb_4Te_4}$ family, X being Ge, Sn, or Pb, by means of the relativistic density functional theory (DFT) calculations.

It is first shown that all three compounds are dynamically stable. Then, on one hand, we find $\mathrm{GeSb_4Te_4}$ and $\mathrm{SnSb_4Te_4}$ to be strong topological semimetals with a large inverted band gap at the Γ-point, while $\mathrm{PbSb_4Te_4}$ is a TI with a narrow band gap of ∼50 meV, all with the $\mathbb{Z}_2$ invariant equal to (1; 000). On the other hand, our mirror Chern number n_M calculations yield topologically nontrivial values (2 for $\mathrm{GeSb_4Te_4}$, but 1 for $\mathrm{SnSb_4Te_4}$ and $\mathrm{PbSb_4Te_4}$), which classifies them as topological crystalline materials as well, revealing their dual topological character. Finally, since the SL blocks in the $X\mathrm{Sb_2Te_4}$ compounds as well as in $\mathrm{GeSb_4Te_4}$ feature cation (X-Sb) intermixing, we investigate its effect on the topology, as exemplified by $\mathrm{GeSb_4Te_4}$ and $\mathrm{PbSb_4Te_4}$, and conclude that the dual topological state is robust against this intermixing.

II. RESULTS AND DISCUSSION

A. Structural properties

In the experiment, so far only $\mathrm{GeSb_4Te_4}$ was synthesized (in both powder and single crystal forms) and found to crystallize in the $P\bar{3}m1$ space group structure [23]. Its lattice constants were determined to be $a \simeq 4.247$ Å and $c \simeq 17.483$ Å. The unit cell can be formally considered as being made of an SL block of $\mathrm{GeSb_2Te_4}$ and a BL of Sb, as shown in Fig. 1(a). The bonding between the SLs and BLs is not purely of the van der Waals (vdW) nature, as in $\mathrm{Sb_2Te_3}$ or $\mathrm{GeSb_2Te_4}$: according to Ref. [23], the Te-Sb distance across

TABLE I. Optimized cell parameters a and c as well as the interlayer distances d_i, as indicated in Fig. 1(a). $d_{\mathrm{Te-Sb}}$ is the Te-Sb interatomic distance across the SL-BL spacing. All values are given in Å.

	a	c	d_1	d_2	d_3	d_{vdW}	d_4	$d_{\mathrm{Te-Sb}}$
$GeSb_4Te_4$	4.275	16.992	1.721	1.975	1.654	2.360	1.571	3.415
$SnSb_4Te_4$	4.332	17.190	1.686	1.952	1.871	2.314	1.543	3.407
$PbSb_4Te_4$	4.352	17.313	1.670	1.922	1.990	2.307	1.533	3.411

the SL-BL spacing (3.497 Å) is significantly shorter than the sum of the Sb and Te vdW radii (Sb: 2.00 Å, Te: 2.06 Å), which indicates partial covalent bonding.

Furthermore, our calculations for interactions between Te and Sb atoms at the SL-BL boundary in $GeSb_4Te_4$ and those across the vdW spacing (Te-Te) in the parent SL-only-based $GeSb_2Te_4$ compound, made using the projected crystal orbital Hamilton population method [24–26], are in line with this. Indeed, we find that the Te-Sb bond is more than two times stronger than that between Te atoms bordering the vdW spacing in the parent compound: 0.59 vs 0.25 eV, respectively. At the same time, this Te-Sb bond across the SL-BL spacing is the weakest in $GeSb_4Te_4$, where the bond strengths for the Sb-$Te_{\mathrm{out/in}}$, Te-Ge, and Sb-Sb pairs are respectively equal to 1.98/1.25, 1.77, and 2.71 eV (the latter corresponds to the interaction within the BL). Despite the SL-BL interaction in $GeSb_4Te_4$ being about two times stronger than the vdW interaction in the parent $GeSb_2Te_4$ compound, we will nevertheless refer to the SL-BL spacing as the vdW gap since it is significantly larger than any other interlayer distance of the $X Sb_4Te_4$ compounds (Table I).

Similarly to $GeSb_2Te_4$ and $Ge_2Sb_2Te_5$ [23,27,28], the SLs of $GeSb_4Te_4$ show mixed occupancy of the cation sites (Ge and Sb) according to the available experimental data. Namely, the central atomic layer of each SL is randomly occupied by Ge and Sb atoms in the 0.5/0.5 ratio, while the peripheral cation layers have the $Sb_{0.75}Ge_{0.25}$ composition [23]. Te and the BL Sb sites do not show fractional site occupancy.

To the best of our knowledge, $SnSb_4Te_4$ and $PbSb_4Te_4$ have not been synthesized yet. However, since the $X Sb_2Te_4$ phases exist for all X (= Ge, Sn, Pb) [29], the existence of $GeSb_4Te_4$ indicates that experimental realization of the isostructural Sn- and Pb-based $X Sb_4Te_4$ compounds is highly likely, too.

We will first neglect the X-Sb intermixing and study the electronic structure and topology of the ideal $X Sb_4Te_4$ compounds. Next, the effect of the intermixing on these properties will be assessed, as exemplified by $GeSb_4Te_4$, for which the structural data are available from the experiment, as well as $PbSb_4Te_4$ for which we assume the same intermixing ratios as for $GeSb_4Te_4$.

Full structural optimization (cell volume, c/a ratio, and atomic positions) of the ideal bulk $P\bar{3}m1$ $X Sb_4Te_4$ yields structures with the parameters listed in Table I. The theoretically optimized a (c) lattice parameter of $GeSb_4Te_4$ is 0.66% larger (2.8% smaller) than the experimental one, which we consider as a reasonable agreement, especially taking into account that the intermixing is neglected in the calculation. We therefore expect that the lattice parameters of $SnSb_4Te_4$ and $PbSb_4Te_4$ are also determined reasonably well.

Next, we study the dynamic stability of the compounds of the $X Sb_4Te_4$ family in their ideal structure. Figures 1(c)–1(h) show the calculated phonon dispersions and the corresponding densities of states (DOS) for all three systems under consideration. For $GeSb_4Te_4$, low-energy vibrations are mainly associated with displacements of Sb and Te atoms, which is due to their differences in mass with Ge. In the $SnSb_4Te_4$ compound there is no such difference between Sb, Te, and Sn, while in the case of $PbSb_4Te_4$, the modes that determine the low-energy part of the phonon spectrum are associated with vibrations of heavy Pb atoms. Overall, there are no anomalies in the dispersion of phonons and all phonon modes have positive frequencies, which indicates the dynamical stability of the ideal $X Sb_4Te_4$ compounds. At the same time, the partial Sb-BL DOS for all three systems demonstrates a gap of about 5 meV between the low-frequency vibration modes, which are hybridized with Te vibrations, and high-frequency modes localized within the BL. The existence of the gap indicates a relatively weak, vdW-like bonding between the Sb BL and the SL, while the presence of the hybrid low-frequency vibration modes is in line with a partially covalent character of the Sb-Te bond across the vdW gap.

B. Electronic properties

1. Bulk band structure and topology

Now, we turn to the characterization of the electronic properties of $X Sb_4Te_4$, first within the ideal crystal structure model. The bulk band structures, calculated along the high-symmetry path K-Γ-M-K-H-A-L-H of the 3D Brillouin zone (BZ) and taking SOC into account, are shown in Fig. 2. Within the generalized gradient approximation (GGA), all compounds turn out to be semimetallic (see Supplemental Material (SM) Fig. S1 [30]), featuring several small electron and hole pockets throughout the BZ. These pockets are seen along the high-symmetry directions for $GeSb_4Te_4$ and $SnSb_4Te_4$ in Figs. 2(a) and 2(b), but appear out of those directions in $PbSb_4Te_4$ [i.e., they are not seen in Fig. 2(c)]. Overall, the electronic state dispersions of the $X Sb_4Te_4$ compounds are similar to one another and appear to be much more complex than those of the parent $X Sb_2Te_4$ systems [31], reflecting the more complex atomic structure of the former.

Detailed band structure analysis of $X Sb_4Te_4$ can be found in Notes S3 and S4 of the SM [30], while here, we summarize its most important conclusions. Near the BZ center, both the valence band (VB) maximum and conduction band (CB) minimum of $X Sb_4Te_4$ are mainly formed by the same type of the orbitals–X-$p_{x,y,z}$ and Sb_{SL}-$p_{x,y,z}$, although the Sb_{BL}-$p_{x,y}$ and Te_{out}-$p_{x,y}$ states contribute as well, especially in $GeSb_4Te_4$. However, the orbital characters of the low-energy bands are so complex that their analysis does not allow one to judge whether the bulk band gap is inverted or not. To address this issue, we have artificially varied the separation between the $X Sb_4Te_4$ SL and Sb, as was previously done to analyze the bulk, surface and interface bands of different systems [11,32,33], and found that in all three systems, there is indeed a bulk band gap inversion at the Γ-point. Remarkably, this inversion is driven by hybridization between the SL and BL

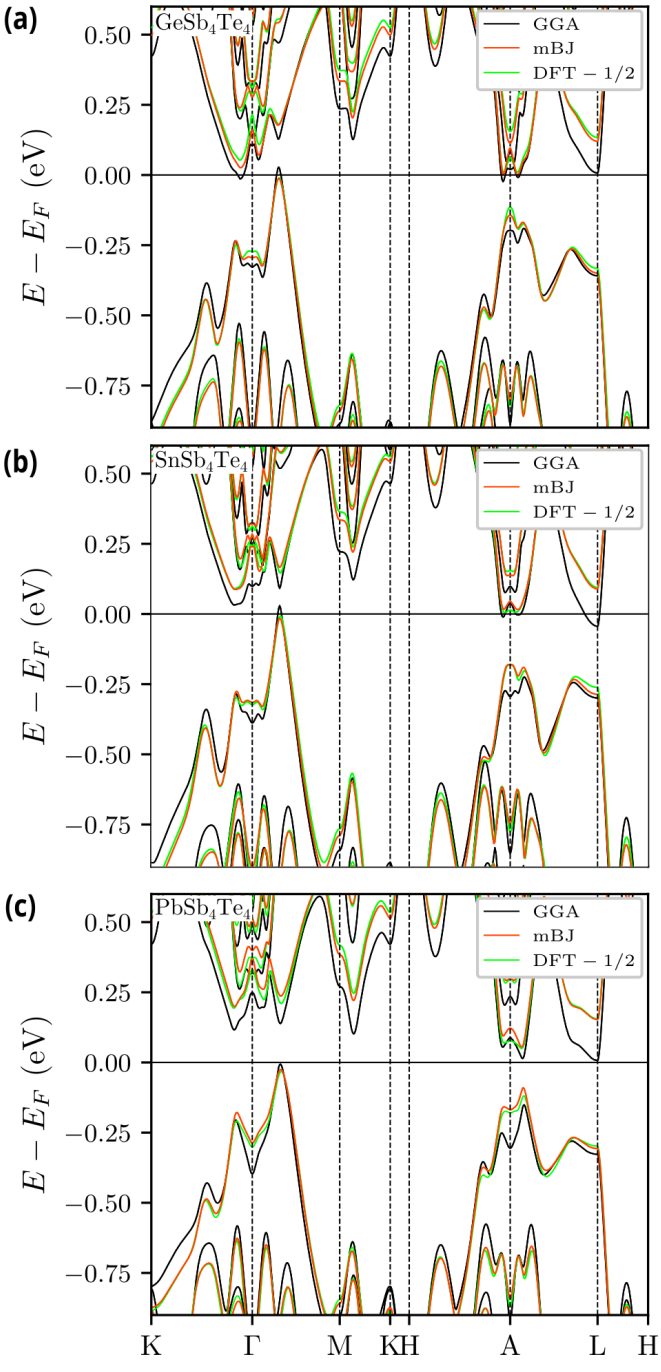

FIG. 2. Bulk band structures calculated for the ideal (a) $GeSb_4Te_4$, (b) $SnSb_4Te_4$, and (c) $PbSb_4Te_4$ along the high symmetry path denoted in Fig. 1(b) and taking SOC into account. The dispersions shown in black, red, and green correspond to the GGA, mBJ, and DFT-1/2 levels of description, respectively. See the main text and the methods section for details.

and appears even without SOC, whereby the band structures resemble the nodal-line semimetals [34,35]. This band gap inversion suggests a nontrivial topology of all compounds of the XSb_4Te_4 family. They feature both the TRS and the reflection symmetry with respect to the $\{11\bar{2}0\}$ mirror planes and, thus, both the $\mathbb{Z}_2$ and topological crystalline states are in principle possible [9,11,36].

TABLE II. The global and Γ-point bulk band gaps of XSb_4Te_4 obtained within the GGA, modified Becke-Johnson (mBJ) potential, and DFT-1/2. All values are given in meV.

Global gap	GGA	mBJ	DFT-1/2
$GeSb_4Te_4$	0.0	0.0	4.5
$SnSb_4Te_4$	0.0	0.0	0.0
$PbSb_4Te_4$	0.0	48.0	43.5
Γ-point gap	GGA	mBJ	DFT-1/2
$GeSb_4Te_4$	431.8	455.6	488.3
$SnSb_4Te_4$	487.1	554.7	566.8
$PbSb_4Te_4$	645.6	660.4	632.5

Given also the presence of the inversion symmetry in the XSb_4Te_4 family, we calculate the $\mathbb{Z}_2$ invariant based on the parity products in the time reversal invariant momenta (TRIM) using the Fu-Kane formula [37]. The TRIM of these systems are shown in Fig. 1(b) and the calculated parity products at TRIM are listed in Table S1 of the SM [30]. Furthermore, we also calculate this invariant by means of the Wannier charge center summation [38]. Both of these methods yield $\mathbb{Z}_2$ of (1; 000) for all three systems, which reveals their strong topological character. On the other hand, the mirror Chern number [39,40] calculation yields $n_M = 2$ for $GeSb_4Te_4$ and $n_M = 1$ for the other two compounds, which also classifies them as topological crystalline materials. We believe that the difference in the mirror Chern number should be a consequence of the different orbital compositions of the occupied bands in $GeSb_4Te_4$ compared to the other two materials (see detailed discussion in Note S5 of the SM [30]).

We further find that the obtained semimetallic state in calculations with SOC included may be a consequence of the deficiencies inherent in the GGA. When the spectrum is calculated on the meta-GGA level within the modified Becke-Johnson (mBJ) potential approximation, which is better suited for the band gap description, a gap of 48 meV appears in $PbSb_4Te_4$. Moreover, as seen in Fig. 2 (red lines), the electron and hole pockets seen along the high-symmetry directions are moved away from the Fermi level in all compounds. For $GeSb_4Te_4$ and $SnSb_4Te_4$, however, there are several remaining pockets elsewhere in the BZ, so that they stay semimetallic (see Fig. S1 of the SM [30]). On the other hand, the use of meta-GGA does not affect the band gap inversion in the Γ-point, the corresponding gap increasing compared to the GGA result (Table II). According to our calculations, the $\mathbb{Z}_2$ invariant turns out to be exactly the same within the mBJ approximation for all XSb_4Te_4, which can also be expected for the mirror Chern number.

To conclude the discussion of the bulk electronic properties, the XSb_4Te_4 (X = Ge, Sn) compounds with the ideal crystal structure turn out to be dual topological semimetals, while $PbSb_4Te_4$ is a dual narrow-gap TI. The topology is robust with respect to both the density functional theory method (we used the PAW, FLAPW, LCAO, and KKR methods, see Sec. V. *Computational details* for computational parameters and Notes S6 and S7 of the SM [30] for the comparison of bulk bands of $GeSb_4Te_4$ obtained with these methods) and the exchange and correlation potential used (GGA and mBJ).

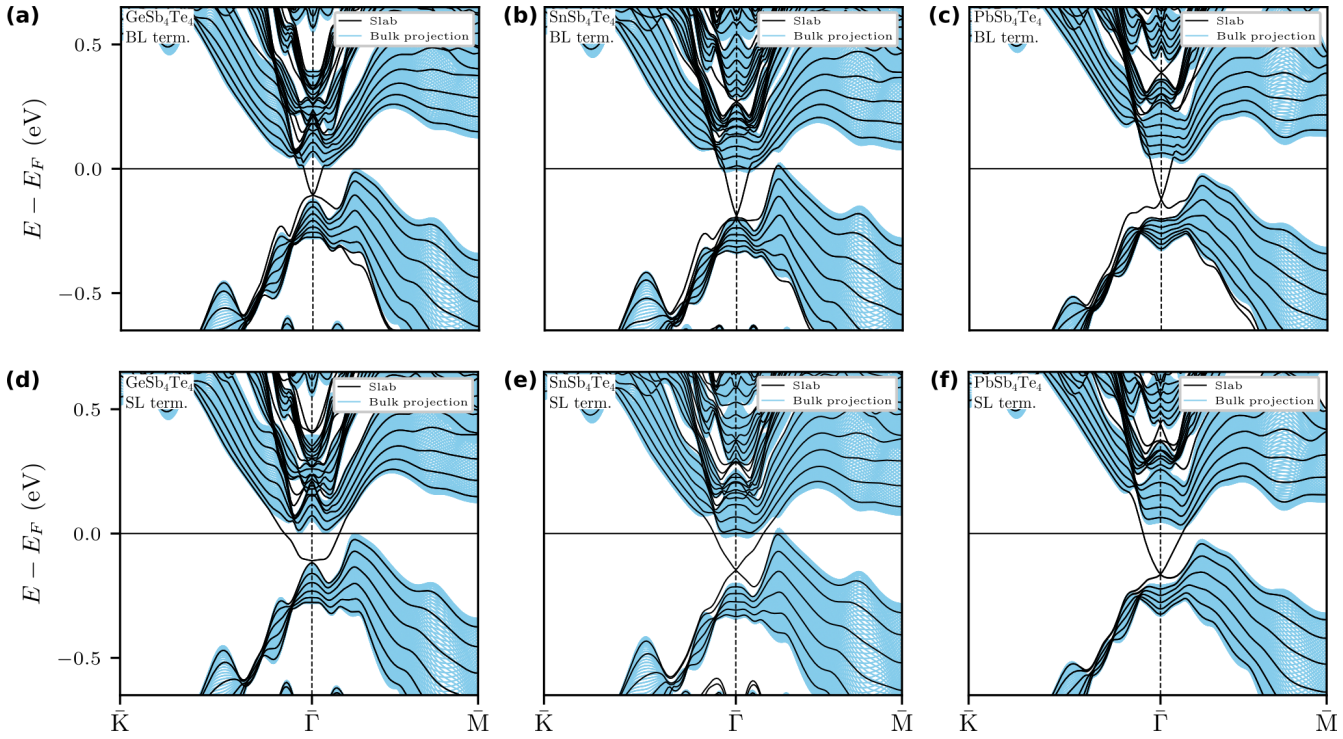

FIG. 3. Band structures for the BL [(a),(b),(c)] and SL [(d),(e),(f)] terminated (0001) surface of $GeSb_4Te_4$ [(a),(d)], $SnSb_4Te_4$ [(b),(e)], and $PbSb_4Te_4$ [(c),(f)].

2. *Surface band structure*

Since the calculated $\mathbb{Z}_2$ invariant suggests that all materials in the XSb_4Te_4 (X = Ge, Sn, Pb) family feature a strong topology, they should feature the TSS that traverses the band gap on any surface cut. On the other hand, the nonzero mirror Chern number indicates that one should expect the TSS on the surface perpendicular to the mirror planes. This means that the TSS at the (0001) surface of XSb_4Te_4 should be protected by both these symmetries.

Given that the mBJ approach cannot be used for slab calculations, to obtain the surface spectra we resort to the computationally efficient DFT-1/2 method, which has been successfully applied to a number of systems, in particular, topological ones [41]. As described in the *Computational details* section, we construct the DFT-1/2 pseudopotentials in such a way that the mBJ band structure is reproduced to a great extent (see Fig. 2 [green lines], Table II and Note S1 of the SM [30]). In particular, we make sure that these pseudopotentials preserve the $\mathbb{Z}_2$ invariant of (1; 000) for all three systems.

Because the coupling between the SL and BL is weaker than the coupling within these layers, we assume that in the experiment the (0001) plane cut would likely be realized by cleaving the bulk crystal along the vdW gap between these two blocks. This would expose a surface with two different terminations, SL and BL, that are anticipated to have different TSS dispersions.

Figure 3 shows the calculated XSb_4Te_4(0001) slab bands overlaid on the projections of bulk bands onto the 2D BZ for all three compounds and both terminations. The TSS of the BL terminations [Figs. 3(a)–3(c)] show rather similar shapes, with a linear dispersion and high group velocity of the upper part, but with a quite unusual dispersion of the lower part. The reason for the latter is illustrated in Movies 5 and 6 of the SM [30], which show the evolution of the surface band structure upon tuning the SOC constant from zero to its natural value for $GeSb_4Te_4$ and $PbSb_4Te_4$, respectively (the situation in $SnSb_4Te_4$ is analogous to that in $PbSb_4Te_4$). It can be seen that without SOC, the BL termination features trivial surface states in the VB, both around the $\overline{\Gamma}$-point (at about −0.2 eV in all cases) and along the $\overline{\Gamma} - \overline{K}$ directions. These states appear presumably due to the breaking of a (partially) covalent bond between the BL and SL upon the surface formation. As shown in the SM Movies, upon adiabatic tuning of SOC, these states first become spin split and then interact with the TSS, eventually leading to the formation of the complex dispersion of the lower part of the TSS observed in Figs. 3(a)–3(c).

On the other hand, at the SL terminations, a striking difference in dispersions between $GeSb_4Te_4$, with its U-like upper part of the TSS, and the other two compounds, showing a more usual X-like behavior of the TSS, is seen [Figs. 3(d)–3(f)]. In Movie 7 of the SM, one can trace back how this non-linear dispersion of $GeSb_4Te_4$'s TSS arises. Along $\bar{\Gamma} - \bar{K}$, the nonlinearity is probably related to both the shape and overlap of the $GeSb_4Te_4$ valence and conduction bands around the $\overline{\Gamma}$-point. On the other hand, along $\bar{\Gamma} - \bar{M}$ the deviation from a linear law is caused by the interaction of the nascent TSS with the drumhead-like state shown in Fig. S4(b) of the SM [30], which is absent in $SnSb_4Te_4$ and $PbSb_4Te_4$. Incidentally, at the BL termination, the latter state also affects the TSS dispersion along $\bar{\Gamma} - \bar{M}$, introducing certain differences in the behavior of the lower part of the $GeSb_4Te_4$ TSS

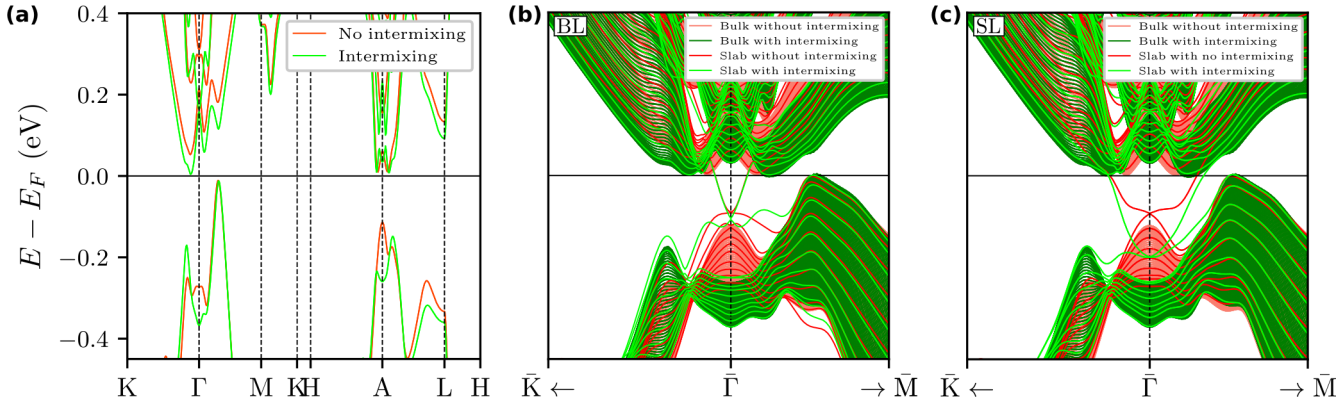

FIG. 4. (a) Bulk band structure of $GeSb_4Te_4$ with (green) and without (red) Ge-Sb intermixing. [(b),(c)] Band structures for the BL (b) and SL (c) terminations of the $GeSb_4Te_4$ (0001) surface without (reddish colors) and with (greenish colors) the Ge-Sb intermixing. The calculations are done within VCA approximation using the DFT-1/2 pseudopotentials. In these calculations, the central atomic layer of each SL is randomly occupied by Ge and Sb atoms in the 0.5/0.5 ratio, while the peripheral cation layers have the $Sb_{0.75}Ge_{0.25}$ composition [23].

as compared to $SnSb_4Te_4$ and $PbSb_4Te_4$ (c.f. SM Movies 5 and 6).

3. Effect of intermixing on electronic properties

As stated previously, it was determined experimentally [23] that in $GeSb_4Te_4$ there is intermixing between the Ge and Sb atoms in the SL. Moreover, such an intermixing was also observed in XSb_2Te_4 systems, with similar ratios to $GeSb_4Te_4$[29]. Thus, it can be expected that intermixing with the same ratios would also happen in Sn- and Pb-based XSb_4Te_4 compounds. We therefore explore the effect of this intermixing on the electronic structure and topology, taking $GeSb_4Te_4$ and $PbSb_4Te_4$ as examples. For this purpose, we used the same crystal structure as for the case with no intermixing (i.e., the theoretically optimized one, see Sec. II A), which is done to explore the effect of the mixing alone, without other factors contributing.

We start with calculating the bulk band structure of $GeSb_4Te_4$ with Ge-Sb intermixing, using both the virtual crystal approximation (VCA) within VASP and coherent potential approximation (CPA) within the Green's function method code HUTSEPOT, using GGA in both cases (see *Computational details* section). Our purpose here is to check the VCA reliability for the XSb_4Te_4, in which two rather dissimilar elements, Ge and Sb, are mixed. The results of VCA and CPA calculations show a reasonable agreement (see Note S7 in the SM [30]), and therefore VCA was used in further calculations as it is computationally more efficient.

We now pass to the DFT-1/2 approximation and compare the $GeSb_4Te_4$ bulk band structures with and without intermixing, as shown in Fig. 4(a). The band dispersions turn out to be rather similar in these two cases. However, around the Γ- and *A*-points, certain qualitative changes are seen both in the bulk VB and bulk CB. The analysis of the orbital composition of the bands that changed their dispersions reveals that all of them feature significant Ge and Sb_{SL} contributions, which explains the observed changes. Overall, the DFT-1/2-calculated bulk spectrum of $GeSb_4Te_4$ appears to be gapless when the intermixing is taken into account, as it can be seen by the behavior of the bulk bands projection onto the 2D BZ [Figs. 4(b) and 4(c)]. On the other hand, the parity products in the TRIM and, hence, the $\mathbb{Z}_2$ invariant remains the same as in the ideal $GeSb_4Te_4$, meaning that it retains the $\mathbb{Z}_2$ topological nature. As for the mirror symmetry, required for the topological crystalline phase, in a system with disorder it is preserved in a globally averaged sense [42] and hence $GeSb_4Te_4$ stays nontrivial. Thus, the dual topologically nontrivial state in $GeSb_4Te_4$ is robust against the Ge-Sb intermixing. The results for $PbSb_4Te_4$ are presented in Note S8 of the SM [30], leading to conclusions that are analogous, i.e., the intermixing does not affect the nontrivial topology, with a note that it leads to a slight increase of the bulk band gap. One can therefore expect that the dual topology of $SnSb_4Te_4$ will not be affected by the intermixing either.

Figures 4(b) and 4(c) show the calculated surface electronic structure of $GeSb_4Te_4$ with Ge-Sb intermixing, where the spectra for the ideal case are shown for comparison. It can be seen that the intermixing affects the dispersion of the TSS at both terminations. The most striking change occurs at the SL termination, where a rather flat (around $\bar{\Gamma}$) upper part of the TSS of the ideal system transforms into the one dispersing with a much higher group velocity when the intermixing is taken into account. Note that such strong changes are revealed not only in the VCA-DFT-1/2 surface electronic structure calculations but also in those within VCA-GGA (not shown).

III. CONCLUSIONS

In this work, we have explored the XSb_4Te_4 materials (X = Ge, Sn, Pb) using the relativistic density functional theory calculations. While only $GeSb_4Te_4$ has been synthesized up to this moment, our results suggest that all three compounds should be dynamically stable, given that they do not feature any imaginary modes in phonon spectra. Calculations of the electronic structure assuming the ideal crystal structure model (i.e., neglecting the experimentally found cation intermixing) show that these materials display dual topology, i.e., they are both time-reversal symmetric topological materials with $\mathbb{Z}_2$ invariant of (1;000) and mirror symmetric topological materials with the mirror Chern number of 2 for $GeSb_4Te_4$ and 1 for $SnSb_4Te_4$ and $PbSb_4Te_4$. However, only

$PbSb_4Te_4$ shows a gapped spectrum with a band gap of about 50 meV, while $GeSb_4Te_4$ and $SnSb_4Te_4$ are semimetallic. Note that this semimetallicity does not endanger the dual topology, as the latter stems from the robust band inversion around the Γ-point, at which the band gap reaches several hundreds of meV. Moreover, we further confirm that the dual topology of XSb_4Te_4, revealed in the ideal case, also persists when the cation (X-Sb) intermixing is taken into account.

ACKNOWLEDGMENTS

We thank Z.S. Aliev, D. Sánchez-Portal, and G. Bihlmayer for insightful discussions. We also thank G. Bihlmayer for providing the subroutine for the mirror Chern number calculations. M.B., M.M.O., and I.Yu.S. acknowledge the support of MCIN/AEI/10.13039/501100011033/ (Grant No. PID2022-138210NB-I00) and "ERDF A way of making Europe." M.M.O. also acknowledges the support of Ayuda CEX2023-001286-S financiada por MICIU/AEI/10.13039/501100011033, as well as MCIN with funding from the European Union NextGenerationEU (PRTR-C17.I1) promoted by the Government of Aragon. A.Yu.V. acknowledges support from the Ministry of Science and Higher Education of the Russian Federation (State Task No. FSWM-2020-0033). S.V.E. and Yu.M.K. acknowledge the support of the Government research assignment for ISPMS SB RAS, Project No. FWRW-2022-0001. We also acknowledge Saint-Petersburg State University for a research project 116812735. R.M.G. acknowledges support from the Swedish Research Council (VR starting Grant No. 2022-03350), the Olle Engkvist Foundation (Grant No. 229-0443), the Royal Physiographic Society in Lund (Horisont), the Knut and Alice Wallenberg Foundation (Grant No. 2023.0087), and Chalmers University of Technology, via the department of physics and the Areas of Advance Nano and Materials. A.E. acknowledges funding by Fonds zur Förderung der Wissenschaftlichen Forschung (FWF) Grant No. I 5384.

APPENDIX: COMPUTATIONAL DETAILS

The first-principles calculations were performed using DFT as implemented in different codes, as detailed below. In most of the calculations, the generalized gradient approximation (GGA) to the exchange-correlation functional was that of Perdew, Burke, and Ernzerhof (PBE) [43], unless explicitly stated otherwise.

VASP calculations. The structural optimization as well as the bulk and surface electronic structure were calculated using the Vienna Atomic Simulation Package (VASP) [44–47] within the projector augmented-wave (PAW) method [48,49]. The accurate cell parameters and atomic positions of bulk cells required for phonon spectra calculations were obtained using VASP's built-in conjugate gradient algorithm. Van der Waals corrections were taken into account using the DFT-D3 approach [50]. The plane wave cutoff was set to 460 eV. The electronic convergence threshold was 10^{-7} eV, while the ionic convergence threshold was 10^{-5} eV/Å. The first Brillouin zone (BZ) was sampled by $13 \times 13 \times 4$ Γ-centered Monkhorst-Pack grid and the occupations of electronic states were smeared according to the Gaussian function of the width of 10 meV. The spin-orbit coupling (SOC) was taken into account, as implemented in VASP, and the symmetry reduction of the number of k-points was disabled.

For the static self-consistent calculations in bulk, the $13 \times 13 \times 4$ Γ-centered Monkhorst-Pack sampling of the first BZ and tetrahedron integration method of Blöchl were used. The plane wave cutoff was reduced to 230 eV and the electronic convergence threshold was loosened to 10^{-6} eV.

The PBE calculations were extended to a meta-GGA level by using the modified Becke-Johnson (mBJ) potential [51,52] approach as implemented in VASP. In all calculations, the initial mBJ potential was constructed from the converged PBE charge density and wave functions using the default mBJ potential parameters. To guarantee the accuracy of this approach, a minimum of 70 self-consistent steps were used, adjusting upward if necessary. All numerical parameters were otherwise equal to the ones in the PBE calculations.

The accurate DOS was obtained by the Wannier interpolation of the results obtained in the self-consistent calculations, on a $150 \times 150 \times 150$ Γ-centered Monkhorst-Pack grid.

For the surface band structure calculations, we apply the Slater-type DFT-1/2 self-energy correction method [53,54] which only requires the addition of a self-energy correction potential, calculated from a partially ionized free atom, to the standard DFT potential (PAW-PBE, in our case). In this case, the ionization level ($-1/2e$ by default) can be an additional variable parameter for fitting the band structure. This method yields accurate band structures for many semiconductors and topological insulators [41] and owing to its low computational cost DFT-1/2 can be considered as a good alternative to semilocal mBJ exchange potential, which diverges for surface calculations, and to any other expensive and time-consuming computational schemes. Before using the DFT-1/2 method for surface calculation we compared its results with the bulk mBJ spectra. For XSb_4Te_4 compounds, the best agreement with the mBJ spectra was obtained with quaternary ionization of both tellurium and antimony potentials. At the same time, the modification of the X potential does not affect the bands near the Fermi level.

The XSb_4Te_4 surfaces were simulated within a model of repeating films separated by a vacuum gap of a minimum of 10 Å. For $SnSb_4Te_4$ and $PbSb_4Te_4$ 61- and 65-atomic-layers-thick inversion symmetric slabs were used for the SL- and BL-terminated surfaces, respectively. For $GeSb_4Te_4$, thicker slabs were used (88- and 92-layer-thick, respectively) to reduce the splitting of the TSS Dirac point due to the interaction between the slab's surfaces. For both surface terminations, the interlayer distances were optimized for the utmost blocks (BL or SL) using the ionic convergence threshold of 10^{-2} eV/Å. The other computational parameters were kept the same as for the static bulk calculations. The 2D BZ was sampled with the $13 \times 13 \times 1$ k-mesh. The static slab calculations were performed for the optimized slabs within the DFT-1/2 approach.

The virtual crystal approximation (VCA) calculations were performed as implemented in VASP [55,56], using the experimentally determined site occupancies for $GeSb_4Te_4$ [23]. Systems constructed for VCA calculations cannot be optimized in VASP, so the optimized cell parameters and atomic

positions for $GeSb_4Te_4$ without the intermixing were used. As we failed to Wannierize the bulk electronic structures within VCA, the band gap sizes were estimated from the electronic densities of states (DOS) that were obtained by an additional non-self-consistent calculation with a denser $35 \times 35 \times 9$ Γ-centered Monkhorst-Pack sampling (both for the ideal and the intermixing case).

Phonon calculations. Phonon spectra calculations were carried out within the framework of DFT with relativistic norm-conserving pseudopotentials constructed from all-electron valence states according to the Vanderbilt scheme [57]. The exchange and correlation energy functional was described within the GGA-PBE. The lattice dynamics of XSb_4Te_4 compounds were studied using a linear response approach based on the DFT as implemented in the mixed-basis pseudopotential method [58,59], which employs a combination of local functions and plane waves to represent valence states [60]. SOC was treated fully self-consistently [61]. We used a kinetic energy cutoff of 24 Ry, while the integrations over the BZ were performed using a $12 \times 12 \times 4$ k-point mesh combined with a Gaussian broadening with a smearing parameter of 0.1 eV. The dynamical matrices were computed on a $6 \times 6 \times 2$ q-point grid and then a Fourier interpolation scheme was used to obtain phonon frequencies along high-symmetry directions of the BZ.

FLEUR calculations. Additional bulk electronic structure calculations were performed within the full-potential linearized augmented plane waves (FLAPW) formalism [62] as implemented in FLEUR [63] to calculate the mirror Chern number. These calculations were performed at the level of PBE, using the optimized VASP crystal structure without a relaxation of atomic positions. The product of the muffin tin-radii, R_{MT}, and plane-wave cutoff, k_{max}, was chosen to be 10. The l-expansion cutoff in the muffin tins, l_{max}, was 10. The k-point grid for self-consistent field calculation was $7 \times 7 \times 2$. Then, for the purpose of determination of the mirror Chern number, Wannierization was performed with $5 \times 5 \times 5$ k-point grid (also tested against $10 \times 10 \times 5$). Thereby, p- and d-states of all atoms were taken into account. The MCN was calculated using WannierTools code with a slightly modified routine to change m_z to m_x or m_y.

HUTSEPOT calculations. To describe the Ge-Sb intermixing in $GeSb_4Te_4$, we have also used the HUTSEPOT code [64] based on the Green function method within the multiple scattering theory [65,66]. The cation intermixing was modeled by mixing two atomic species on the same atomic site within the coherent potential approximation (CPA) [67,68]. The experimentally determined site occupancies for $GeSb_4Te_4$ [23] were adopted. The crystal structures optimized by VASP were used.

Symmetry analysis. To extract the symmetry information of the $GeSb_4Te_4$ and $PbSb_4Te_4$ bands, we calculated the band structure in QuantumESPRESSO package [69–71] within the projector augmented wave method [48,72] and GGA-PBE. These calculations were performed both with and without SOC taken into account. In both cases, the cell parameters and atomic positions were set to the optimized values obtained in VASP, the wave function cutoff was set to 85 Ry, the charge density cutoff to 680 Ry, and the electronic convergence threshold to 10^{-7} eV. In the static self-consistent calculation the BZ was sampled by $19 \times 19 \times 7$ Monkhorst-Pack grid and the electronic occupations were treated by Blöchl's tetrahedron integration method [73], while for the band structure calculation, Marzari-Vanderbilt smearing [74] of 0.1 Ry was used instead. The symmetry information was then taken from the bands.x routine output. Additional symmetry analysis was performed using the GTPack [75,76].

Wannier calculations. Wannier functions required to calculate the $\mathbb{Z}_2$ invariants by the Wannier charge centers method [38] were obtained by the Wannier90 code [77,78]. The Wannier charge center summation was performed by WannierTools code [79]. The surface spectral functions shown in Figs. S4 and S10 of the SM [30] were calculated by the Green function method [80] from the tight-binding Wannier Hamiltonian as implemented in WannierTools [79].

SIESTA-GREEN calculations. The $GeSb_4Te_4$ surface spectral functions in Movies 5, 6, and 7 of the SM were obtained using the GREEN code [81] and its interface to the DFT SIESTA [82] package. The crystal structures optimized by VASP were used. In the first step, self-consistent Hamiltonians for all supercells were computed using SIESTA within the GGA-PBE approximation to the exchange-correlation potential and including SOC via the fully relativistic pseudopotential approach [83]. The core electrons were described by norm-conserving pseudopotentials of the Troulliers-Martin type, with core corrections included for all atoms. With this approach, we obtain a good agreement between the bulk spectra calculated using SIESTA and VASP. A Green function-based approach was followed in order to model the surface as a semi-infinite medium [81].

[1] C. L. Kane and E. J. Mele, Z_2 topological order and the quantum spin Hall effect, Phys. Rev. Lett. **95**, 146802 (2005).

[2] L. Fu, C. L. Kane, and E. J. Mele, Topological insulators in three dimensions, Phys. Rev. Lett. **98**, 106803 (2007).

[3] M. Z. Hasan and C. L. Kane, *Colloquium:* Topological insulators, Rev. Mod. Phys. **82**, 3045 (2010).

[4] X.-L. Qi and S.-C. Zhang, Topological insulators and superconductors, Rev. Mod. Phys. **83**, 1057 (2011).

[5] A. Bansil, H. Lin, and T. Das, *Colloquium:* Topological band theory, Rev. Mod. Phys. **88**, 021004 (2016).

[6] B. A. Bernevig, C. Felser, and H. Beidenkopf, Progress and prospects in magnetic topological materials, Nature (London) **603**, 41 (2022).

[7] M. M. Otrokov, I. I. Klimovskikh, H. Bentmann, D. Estyunin, A. Zeugner, Z. S. Aliev, S. Gaß, A. U. B. Wolter, A. V. Koroleva, A. M. Shikin *et al.*, Prediction and observation of an antiferromagnetic topological insulator, Nature (London) **576**, 416 (2019).

[8] C.-Z. Chang, C.-X. Liu, and A. H. MacDonald, *Colloquium:* Quantum anomalous Hall effect, Rev. Mod. Phys. **95**, 011002 (2023).

[9] T. Rauch, M. Flieger, J. Henk, I. Mertig, and A. Ernst, Dual topological character of chalcogenides: Theory for Bi_2Te_3, Phys. Rev. Lett. **112**, 016802 (2014).

[10] D. Nabok, M. Tas, S. Kusaka, E. Durgun, C. Friedrich, G. Bihlmayer, S. Blügel, T. Hirahara, and I. Aguilera, Bulk and

surface electronic structure of Bi_4Te_3 from *GW* calculations and photoemission experiments, Phys. Rev. Mater. **6**, 034204 (2022).

[11] M. Eschbach, M. Lanius, C. Niu, E. Młyńczak, P. Gospodarič, J. Kellner, P. Schüffelgen, M. Gehlmann, S. Döring, E. Neumann *et al.*, Bi_1Te_1 is a dual topological insulator, Nat. Commun. **8**, 14976 (2017).

[12] I. P. Rusinov, T. V. Menshchikova, A. Isaeva, S. Eremeev, Y. M. Koroteev, M. Vergniory, P. M. Echenique, and E. V. Chulkov, Mirror-symmetry protected non-TRIM surface state in the weak topological insulator Bi_2TeI, Sci. Rep. **6**, 20734 (2016).

[13] A. P. Weber, Q. D. Gibson, H. Ji, A. N. Caruso, A. Fedorov, R. J. Cava, and T. Valla, Gapped surface states in a strong-topological-insulator material, Phys. Rev. Lett. **114**, 256401 (2015).

[14] Q. Gibson, L. M. Schoop, A. Weber, H. Ji, S. Nadj-Perge, I. Drozdov, H. Beidenkopf, J. Sadowski, A. Fedorov, A. Yazdani *et al.*, Termination-dependent topological surface states of the natural superlattice phase Bi_4Se_3, Phys. Rev. B **88**, 081108(R) (2013).

[15] T. Valla, H. Ji, L. Schoop, A. Weber, Z.-H. Pan, J. Sadowski, E. Vescovo, A. Fedorov, A. Caruso, Q. Gibson *et al.*, Topological semimetal in a Bi-Bi_2Se_3 infinitely adaptive superlattice phase, Phys. Rev. B **86**, 241101(R) (2012).

[16] T. Chagas, O. A. Ashour, G. A. Ribeiro, W. S. Silva, Z. Li, S. G. Louie, R. Magalhães-Paniago, and Y. Petroff, Multiple strong topological gaps and hexagonal warping in Bi_4Te_3, Phys. Rev. B **105**, L081409 (2022).

[17] H.-P. Xue, R. Sun, X. Yang, A. Comstock, Y. Liu, B. Ge, J.-M. Liu, Y.-S. Wei, Q.-L. Yang, X.-S. Gai *et al.*, Dual topology of Dirac electron transport and photogalvanic effect in low-dimensional topological insulator superlattices, Adv. Mater. **35**, 2208343 (2023).

[18] J. Johannsen, G. Autès, A. Crepaldi, S. Moser, B. Casarin, F. Cilento, M. Zacchigna, H. Berger, A. Magrez, P. Bugnon *et al.*, Engineering the topological surface states in the $(Sb_2)_m - Sb_2Te_3$ ($m = 0 - 3$) superlattice series, Phys. Rev. B **91**, 201101(R) (2015).

[19] L. Khalil, E. Papalazarou, M. Caputo, N. Nilforoushan, L. Perfetti, A. Taleb-Ibrahimi, V. Kandyba, A. Barinov, Q. D. Gibson, R. J. Cava *et al.*, Electronic band structure for occupied and unoccupied states of the natural topological superlattice phase Sb_2Te, Phys. Rev. B **95**, 085118 (2017).

[20] Also, note that unlike the Bi BL, the Sb BL is topologically trivial, while the bulk Sb is a strong topological semimetal [39,84,85].

[21] F. Aliyev, E. N. Orujlu, and D. M. Babanly, Synthesis and study of a new mixed-layered compound $GeBi_3Te_4$ belonging to the $nBi_2 - mGeBi_2Te_4$ homologous series, Bull. Univ. Karaganda - Chem. **105**, 92 (2022).

[22] F. Aliyev, Synthesis and study of a novel 9P-type mixed layered tetradymite-like $GeBi_4Te_4$ compound in the Ge-Te-Bi system, Phys. Chem. Solid State **22**, 401 (2021).

[23] M. N. Schneider and O. Oeckler, $GeSb_4Te_4$ – a new 9P-type phase in the system Ge/Sb/Te, Z. Anorg. Allg. Chem. **636**, 137 (2010).

[24] R. Dronskowski and P. E. Bloechl, Crystal orbital Hamilton populations (COHP): energy-resolved visualization of chemical bonding in solids based on density-functional calculations, J. Phys. Chem. **97**, 8617 (1993).

[25] V. L. Deringer, A. L. Tchougréeff, and R. Dronskowski, Crystal orbital Hamilton population (COHP) analysis as projected from plane-wave basis sets, J. Phys. Chem. A **115**, 5461 (2011).

[26] S. Maintz, V. L. Deringer, A. L. Tchougréeff, and R. Dronskowski, LOBSTER: A tool to extract chemical bonding from plane-wave based DFT, J. Comput. Chem. **37**, 1030 (2016).

[27] S. Eremeev, I. P. Rusinov, P. M. Echenique, and E. V. Chulkov, Temperature-driven topological quantum phase transitions in a phase-change material $Ge_2Sb_2Te_5$, Sci. Rep. **6**, 38799 (2016).

[28] M. Nurmamat, K. Okamoto, S. Zhu, T. V. Menshchikova, I. P. Rusinov, V. O. Korostelev, K. Miyamoto, T. Okuda, T. Miyashita, X. Wang *et al.*, Topologically nontrivial phase-change compound $GeSb_2Te_4$, ACS Nano **14**, 9059 (2020).

[29] O. Oeckler, M. N. Schneider, F. Fahrnbauer, and G. Vaughan, Atom distribution in $SnSb_2Te_4$ by resonant X-ray diffraction, Solid State Sci. **13**, 1157 (2011).

[30] See Supplemental Material at http://link.aps.org/supplemental/10.1103/PhysRevMaterials.9.014201 for more information.

[31] T. V. Menshchikova, S. V. Eremeev, Y. M. Koroteev, V. M. Kuznetsov, and E. V. Chulkov, Ternary compounds based on binary topological insulators as an efficient way for modifying the Dirac cone, JETP Lett. **93**, 15 (2011).

[32] D. Usachov, A. Fedorov, M. M. Otrokov, A. Chikina, O. Vilkov, A. Petukhov, A. G. Rybkin, Y. M. Koroteev, E. V. Chulkov, V. K. Adamchuk *et al.*, Observation of single-spin Dirac fermions at the graphene/ferromagnet interface, Nano Lett. **15**, 2396 (2015).

[33] A. Y. Vyazovskaya, M. Otrokov, Y. M. Koroteev, K. Kummer, M. Güttler, D. V. Vyalikh, and E. V. Chulkov, Origin of two-dimensional electronic states at Si- and Gd-terminated surfaces of $GdRh_2Si_2(001)$, Phys. Rev. B **100**, 075140 (2019).

[34] C. Fang, Y. Chen, H.-Y. Kee, and L. Fu, Topological nodal line semimetals with and without spin-orbital coupling, Phys. Rev. B **92**, 081201(R) (2015).

[35] C. Fang, H. Weng, X. Dai, and Z. Fang, Topological nodal line semimetals, Chin. Phys. B **25**, 117106 (2016).

[36] J. I. Facio, S. K. Das, Y. Zhang, K. Koepernik, J. van den Brink, and I. C. Fulga, Dual topology in jacutingaite Pt_2HgSe_3, Phys. Rev. Mater. **3**, 074202 (2019).

[37] L. Fu and C. L. Kane, Topological insulators with inversion symmetry, Phys. Rev. B **76**, 045302 (2007).

[38] A. A. Soluyanov and D. Vanderbilt, Computing topological invariants without inversion symmetry, Phys. Rev. B **83**, 235401 (2011).

[39] J. C. Y. Teo, L. Fu, and C. L. Kane, Surface states and topological invariants in three-dimensional topological insulators: Application to Bi_{1-x} Sb_x, Phys. Rev. B **78**, 045426 (2008).

[40] L. Fu, Topological crystalline insulators, Phys. Rev. Lett. **106**, 106802 (2011).

[41] T. Mota, F. Matusalem, M. Marques, L. K. Teles, and I. Guilhon, DFT-1/2 method applied to 3D topological insulators, J. Phys.: Condens. Matter **34**, 465501 (2022).

[42] Y. Ando and L. Fu, Topological crystalline insulators and topological superconductors: From concepts to materials, Annu. Rev. Condens. Matter Phys. **6**, 361 (2015).

[43] J. P. Perdew, K. Burke, and M. Ernzerhof, Generalized gradient approximation made simple, Phys. Rev. Lett. **77**, 3865 (1996).

[44] G. Kresse and J. Hafner, *Ab initio* molecular dynamics for liquid metals, Phys. Rev. B **47**, 558 (1993).

[45] G. Kresse and J. Hafner, *Ab initio* molecular-dynamics simulation of the liquid-metal–amorphous-semiconductor transition in germanium, Phys. Rev. B **49**, 14251 (1994).

[46] G. Kresse and J. Furthmüller, Efficiency of ab-initio total energy calculations for metals and semiconductors using a plane-wave basis set, Comput. Mater. Sci. **6**, 15 (1996).

[47] G. Kresse and J. Furthmüller, Efficient iterative schemes for *ab initio* total-energy calculations using a plane-wave basis set, Phys. Rev. B **54**, 11169 (1996).

[48] P. E. Blöchl, Projector augmented-wave method, Phys. Rev. B **50**, 17953 (1994).

[49] G. Kresse and D. Joubert, From ultrasoft pseudopotentials to the projector augmented-wave method, Phys. Rev. B **59**, 1758 (1999).

[50] S. Grimme, S. Ehrlich, and L. Goerigk, Effect of the damping function in dispersion corrected density functional theory, J. Comput. Chem. **32**, 1456 (2011).

[51] A. D. Becke and E. R. Johnson, A simple effective potential for exchange, J. Chem. Phys. **124**, 221101 (2006).

[52] F. Tran and P. Blaha, Accurate band gaps of semiconductors and insulators with a semilocal exchange-correlation potential, Phys. Rev. Lett. **102**, 226401 (2009).

[53] L. G. Ferreira, M. Marques, and L. K. Teles, Approximation to density functional theory for the calculation of band gaps of semiconductors, Phys. Rev. B **78**, 125116 (2008).

[54] L. G. Ferreira, M. Marques, and L. K. Teles, Slater half-occupation technique revisited: The LDA-1/2 and GGA-1/2 approaches for atomic ionization energies and band gaps in semiconductors, AIP Adv. **1**, 032119 (2011).

[55] L. Bellaiche and D. Vanderbilt, Virtual crystal approximation revisited: Application to dielectric and piezoelectric properties of perovskites, Phys. Rev. B **61**, 7877 (2000).

[56] C. Eckhardt, K. Hummer, and G. Kresse, Indirect-to-direct gap transition in strained and unstrained Sn_xGe_{1-x} alloys, Phys. Rev. B **89**, 165201 (2014).

[57] D. Vanderbilt, Optimally smooth norm-conserving pseudopotentials, Phys. Rev. B **32**, 8412 (1985).

[58] R. Heid and K. P. Bohnen, Linear response in a density-functional mixed-basis approach, Phys. Rev. B **60**, R3709 (1999).

[59] B. Meyer, C. Elsässer, F. Lechermann, and M. Fähnle, FORTRAN90 Program for Mixed-Basis Pseudopotential Calculations for Crystals, Max-Planck-Institut für Metallforschung, Stuttgart (unpublished).

[60] S. G. Louie, K.-M. Ho, and M. L. Cohen, Self-consistent mixed-basis approach to the electronic structure of solids, Phys. Rev. B **19**, 1774 (1979).

[61] R. Heid, K.-P. Bohnen, I. Y. Sklyadneva, and E. V. Chulkov, Effect of spin-orbit coupling on the electron-phonon interaction of the superconductors Pb and Tl, Phys. Rev. B **81**, 174527 (2010).

[62] E. Wimmer, H. Krakauer, M. Weinert, and A. J. Freeman, Full-potential self-consistent linearized-augmented-plane-wave method for calculating the electronic structure of molecules and surfaces: O_2 molecule, Phys. Rev. B **24**, 864 (1981).

[63] FLEUR site: http://www.flapw.de.

[64] M. Hoffmann, A. Ernst, W. Hergert, V. N. Antonov, W. A. Adeagbo, R. M. Geilhufe, and H. Ben Hamed, Magnetic and electronic properties of complex oxides from first-principles, Phys. Status Solidi B **257**, 1900671 (2020).

[65] B. Gyorffy and M. Stott, Theory of soft x-ray emission from alloys, in *Proceedings of the International Conference on Band Structure and Spectroscopy of Metals and Alloys* (Academic Press, New York, 1973).

[66] M. Geilhufe, S. Achilles, M. A. Köbis, M. Arnold, I. Mertig, W. Hergert, and A. Ernst, Numerical solution of the relativistic single-site scattering problem for the Coulomb and the Mathieu potential, J. Phys.: Condens. Matter **27**, 435202 (2015).

[67] P. Soven, Coherent-potential model of substitutional disordered alloys, Phys. Rev. **156**, 809 (1967).

[68] B. L. Gyorffy, Coherent-potential approximation for a nonoverlapping-muffin-tin-potential model of random substitutional alloys, Phys. Rev. B **5**, 2382 (1972).

[69] P. Giannozzi, S. Baroni, N. Bonini, M. Calandra, R. Car, C. Cavazzoni, D. Ceresoli, G. L. Chiarotti, M. Cococcioni, I. Dabo *et al.*, QUANTUM ESPRESSO: A modular and open-source software project for quantum simulations of materials, J. Phys.: Condens. Matter **21**, 395502 (2009).

[70] P. Giannozzi, O. Andreussi, T. Brumme, O. Bunau, M. B. Nardelli, M. Calandra, R. Car, C. Cavazzoni, D. Ceresoli, M. Cococcioni *et al.*, Advanced capabilities for materials modelling with quantum ESPRESSO, J. Phys.: Condens. Matter **29**, 465901 (2017).

[71] P. Giannozzi, O. Baseggio, P. Bonfà, D. Brunato, R. Car, I. Carnimeo, C. Cavazzoni, S. de Gironcoli, P. Delugas, F. Ferrari Ruffino, A. Ferretti, N. Marzari, I. Timrov, A. Urru, and S. Baroni, Quantum espresso toward the exascale, J. Chem. Phys. **152**, 154105 (2020).

[72] A. Dal Corso, Pseudopotentials periodic table: From H to Pu, Comput. Mater. Sci. **95**, 337 (2014).

[73] P. E. Blöchl, O. Jepsen, and O. K. Andersen, Improved tetrahedron method for Brillouin-zone integrations, Phys. Rev. B **49**, 16223 (1994).

[74] N. Marzari, D. Vanderbilt, A. De Vita, and M. C. Payne, Thermal contraction and disordering of the Al(110) surface, Phys. Rev. Lett. **82**, 3296 (1999).

[75] R. M. Geilhufe and W. Hergert, GTPack: A mathematica group theory package for application in solid-state physics and photonics, Front. Phys. **6**, 86 (2018).

[76] W. Hergert and R. M. Geilhufe, *Group Theory in Solid State Physics and Photonics: Problem Solving with Mathematica* (Wiley-VCH, Weinheim, Germany, 2018).

[77] A. A. Mostofi, J. R. Yates, G. Pizzi, Y.-S. Lee, I. Souza, D. Vanderbilt, and N. Marzari, An updated version of Wannier90: A tool for obtaining maximally-localised Wannier functions, Comput. Phys. Commun. **185**, 2309 (2014).

[78] G. Pizzi, V. Vitale, R. Arita, S. Blügel, F. Freimuth, G. Géranton, M. Gibertini, D. Gresch, C. Johnson, T. Koretsune, J. Ibañez-Azpiroz, H. Lee, J.-M. Lihm, D. Marchand, A. Marrazzo, Y. Mokrousov, J. I. Mustafa, Y. Nohara, Y. Nomura, L. Paulatto *et al.*, Wannier90 as a community code: New features and applications, J. Phys.: Condens. Matter **32**, 165902 (2020).

[79] Q. Wu, S. Zhang, H.-F. Song, M. Troyer, and A. A. Soluyanov, WannierTools: An open-source software package for novel topological materials, Comput. Phys. Commun. **224**, 405 (2018).

[80] M. P. L. Sancho, J. M. L. Sancho, J. M. L. Sancho, and J. Rubio, Highly convergent schemes for the calculation of bulk and surface Green functions, J. Phys. F **15**, 851 (1985).

[81] E. T. R. Rossen, C. F. J. Flipse, and J. I. Cerdá, Lowest order in inelastic tunneling approximation: Efficient scheme for simulation of inelastic electron tunneling data, Phys. Rev. B **87**, 235412 (2013).

[82] J. M. Soler, E. Artacho, J. D. Gale, A. García, J. Junquera, P. Ordejón, and D. Sánchez-Portal, The siesta method for *ab initio* order-*N* materials simulation, J. Phys.: Condens. Matter **14**, 2745 (2002).

[83] R. Cuadrado and J. Cerdá, Fully relativistic pseudopotential formalism under an atomic orbital basis: spin–orbit splittings and magnetic anisotropies, J. Phys.: Condens. Matter **24**, 086005 (2012).

[84] D. Hsieh, Y. Xia, L. Wray, D. Qian, A. Pal, J. Dil, J. Osterwalder, F. Meier, G. Bihlmayer, C. Kane *et al.*, Observation of unconventional quantum spin textures in topological insulators, Science **323**, 919 (2009).

[85] P. Zhang, Z. Liu, W. Duan, F. Liu, and J. Wu, Topological and electronic transitions in a Sb(111) nanofilm: The interplay between quantum confinement and surface effect, Phys. Rev. B **85**, 201410 (2012).